TomoSense: a unique 3D dataset over temperate forest combining multi-frequency mono- and bi-static tomographic SAR with terrestrial, UAV and airborne lidar, and in-situ forest census

Stefano Tebaldini[1], Mauro Mariotti d'Alessandro[1], Lars M.H. Ulander[2,3], Patrik Bennet[2], Anders Gustavsson[3], Alex Coccia[4], Karlus Macedo[4], Mathias Disney[5], Phil Wilkes[5], Hans-Joachim Spors[6], Nico Schumacher[6], Jan Hanuš[7], Jan Novotný[7], Benjamin Brede[8,9], Harm Bartholomeus[8], Alvaro Lau[8], Jens van der Zee[8], Martin Herold[8,9], Dirk Schuettemeyer[10], Klaus Scipal[10]

1. Dipartimento di Elettronica, Informazione e Bioingegneria, Politecnico di Milano, Italy
2. Chalmers University of Technology, Sweden
3. Swedish Defence Research Agency (FOI), Sweden
4. MetaSensing, The Netherlands
5. University College London, Gower Street, London, UK; and NERC National Centre for Earth Observation (NCEO), UCL, London, UK.
6. Landesbetrieb Wald und Holz Nordrhein-Westfalen, Germany
7. The Czech Academy of Sciences, Global Change Research Institute (CzechGlobe), Czech Republic
8. Wageningen University & Research, Laboratory of Geo-Information Science and Remote Sensing, Droevendaalsesteeg 3, 6708 PB Wageningen, The Netherlands
9. Helmholtz Center Potsdam GFZ German Research Centre for Geosciences, Section 1.4 Remote Sensing and Geoinformatics, Telegrafenberg, 14473 Potsdam, Germany
10. European Space Agency, European Union

Corresponding author

Stefano Tebaldini

Dipartimento di Elettronica, Informazione e Bioingegneria

Politecnico di Milano

Via Ponzio 34/5

20133, Milano

Italy

Tel: +39 02 2399 3614 Fax: +39 02 2399 3664

Email: stefano.tebaldini@polimi.it

Abstract

The TomoSense experiment was funded by the European Space Agency (ESA) to support research on remote sensing of forested areas by means of Synthetic Aperture Radar (SAR) data, with a special focus on the use of tomographic SAR (TomoSAR) to retrieve information about the vertical structure of the vegetation at different frequency bands. The illuminated scene is the temperate forest at the Eifel National Park, North-West Germany. Dominant species are beech and spruce trees. Forest height ranges roughly from 10 to 30 m, with peaks up to over 40 m. Forest Above Ground Biomass (AGB) ranges from 20 to 300 Mg/ha, with peaks up to over 400 Mg/ha. SAR data include P-, L-, and C-band surveys acquired by flying up to 30 trajectories in two headings to provide tomographic imaging capabilities. L- and C-band data were acquired by simultaneously flying two aircraft to gather bistatic data along different trajectories.

The SAR dataset is complemented by 3D structural canopy measurements made via terrestrial laser scanning (TLS), Unoccupied Aerial Vehicle lidar (UAV-L) and airborne laser scanning (ALS), and in-situ forest census. This unique combination of SAR tomographic and multi-scale lidar data allows for direct comparison of canopy structural metrics across wavelength and scale, including vertical profiles of canopy wood and foliage density, and per-tree and plot-level above ground biomass (AGB). The resulting TomoSense data-set is free and openly available at ESA for any research purpose. The data-set includes ALS-derived maps of forest height and AGB, forest parameters at the level of single trees, TLS raw data, and plot-average TLS vertical profiles. The provided SAR data are coregistered, phase calibrated, and ground steered, to enable a direct implementation of any kind of interferometric or tomographic processing without having to deal with the subtleties of airborne SAR processing. Moreover, the data-base comprises SAR tomographic cubes representing forest scattering in 3D both in Radar and geographical coordinates, intended for use by non-Radar experts. For its unique features and completeness, the TomoSense data-set is intended to serve as an important basis for future research on microwave scattering from forested areas in the context of future Earth Observation missions.

1. Introduction

The introduction of Synthetic Aperture Radar (SAR) tomography has opened the way to new opportunities for microwave remote sensing of forested areas from space (Reigber and Moreira, 2000; Tebaldini et al., 2019). Tomographic SAR surveys require illumination from multiple trajectories to form a data-stack containing multiple SAR images of the same area. The data-stack is then digitally processed to produce a collection of voxels that represent the backscattered energy in three dimensions, thus allowing direct imaging of the interior of the illuminated media (Tebaldini et al. 2017). Space Agencies have increasingly invested in SAR tomography in the last few years, funding activities to assess the use of SAR tomography in the context of spaceborne remote sensing (Aghababaei, 2020; Bloomberg et al., 2021; Tello et al., 2018; Toraño Caicoya et al., 2015; Pardini et al., 2018; Mariotti and Tebaldini, 2019; Kathi et al., 2019; Ho Tong Minh et al., 2014 and 2016; Frey et al., 2008; Fatoyinbo et al., 2021; El Moussawi et al., 2019). As a token of its potential, SAR tomography has been assigned a dedicated 14-month acquisition phase in the context of the forthcoming Earth Explorer mission BIOMASS, to be launched in 2024, (Quegan et al., 2019; Soja et al., 2021), and it has largely been considered in the context of future bistatic missions operating at L-band (Azcueta and Tebaldini, 2020; Moreira et al., 2015; Scipal and Davidson, 2017).

In this context, the TomoSense experiment was organized by the European Space Agency (ESA) to provide the scientific community with unprecedented data to study the features of radar scattering from temperate forests, comprising tomographic and fully polarimetric SAR surveys at P-, L-, and C-band, acquired in mono- and bistatic mode by simultaneously flying two aircraft. The dataset is complemented by a range of dedicated datasets that have proven value in the estimation of above ground biomass (AGB): a detailed forest census, terrestrial laser scanning (TLS) (Disney et al., 2018), mobile laser scanning (MLS) (Mokroš et al., 2021), unoccupied aerial vehicle laser scanning (UAV-LS) (Brede et al., 2017; Brede et al., 2022) and airborne laser scanning (ALS) products (Brovkina et al., 2022).”.

In this paper, we provide a comprehensive overview of the TomoSense experiment and the produced data. The dataset is intended to serve as a basis for future research on microwave scattering from forested areas, as it allows addressing applications such as retrieval of forest height and biomass, along with studying the roles of species diversity and forest vertical structure. The dataset is intended

to be usable without requiring in-depth knowledge of SAR processing, and is freely and openly available through ESA for research purposes

2. The Test site

The test site of TomoSense is located within the Kermeter area in the Eifel National Park in North Rhine-Westphalia, Germany. The site was chosen for its ecological diversity with forest stands of different species, topography and age classes. In addition, being part of a National Park the site is well documented and has an established forest census. The Kermeter is an upland region, up to 528 m above sea level, covered by one of the largest contiguous, deciduous forests in that region. It covers an area of 3,592 hectares, of which about 3,300 hectares is a single forested area (the so-called Kermeter-Hochwald or Kermeter High Forest). Beech woods dominate the shaded, damp northern slopes (24%), in places with trees that are over 200 years old. Oak woods hold sway on the drier, southern slopes (26%), interrupted by rocky outcrops (Felsheide). About 550 hectares consist of spruce trees, which are a consequence of reforestation measures after the Second World War. However, the spruce stock is continuously being reduced by thunderstorms, drought and bark beetle infestations in favour of deciduous woods. A photo of the area is shown in figure 1. The Urft Valley in front / south of the Kermeter was shaped by the meandering Urft River. In 1905 the construction of the Urft Dam was finished and created an Amazon-like reservoir

Fig. 1. The Urft Valley in front / south of the Kermeter area at the Eifel National park, North-West Germany.

The main area of interest targeted by all campaign activities is the one enclosed in the yellow rectangle in figure 2. The area is approximately 6.4 Km long and 800 m wide. Topographic slopes at this area are typically on the order of ±5°, with few areas reaching 10° and beyond.

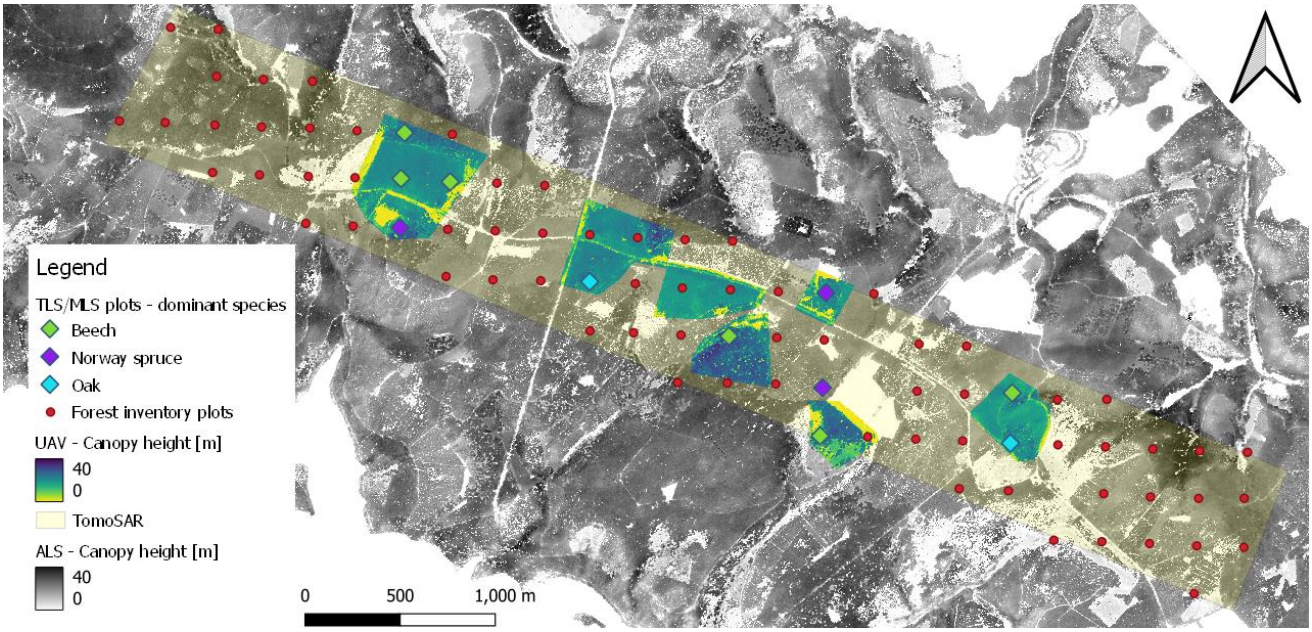

Fig. 2. Graphical overview of the TomoSense campaign.

3. Forest census

Forest census was carried out in spring 2019 to collect several tree parameters. Each parameter was measured at single tree level within 80 plots with size of 0.05 ha (circular plot with radius 12.62 m). The plots are from the permanent inventory established by Wald und Holz in 2011, see figure 2. The distance between any two plots is about 250 m. Each plot centre is marked with a 40 cm long iron nail, and the tree positions are a function of their angle and distance to the plot centre. The position of each plot centre was measured using a Trimble Catalyst DA1 Antenna, which is expected to be accurate to within 1 m. The combination of plot size (500m²) and grid size represents a good compromise between workload and statistical accuracy. At the same time, it allows the use of SAR airborne data to investigate forestr structure at the level of a single plot.

Field data include a total of 2564 sampled trees. For each of these, the following parameters were collected:

- Tree position w.r.t. plot center;
- Diameter at Brest Height (DBH) in mm;
- Height in m;
- Species (ID and name);
- Number of trees per ha;
- Basal area;
- Basal area per hectare.

The data-set is complemented by photographic material including two photos of each plot, see figure 3. In addition an area wide map on the dominant species is available form Wald and Holz.

Landscape *Portrait*

Fig. 3. Landscape and portrait photos of plot 1330 (beech-oak forest).

4. Terrestrial Laser Scanning (TLS)

Collection of TLS data took place in September 2021. The campaign took place under nearly ideal weather conditions with no wind. TLS data were acquired for 11 50 m x 50 m plots. Data was acquired

following a standardized protocol (Wilkes et al. 2017) where scans were acquired on a 16.7 m grid. Individual scans were co-registered using reflective targets, so that the resulting combined plot-level point cloud was accurate to within a few mm. Following co-registration, extraction of individual trees was carried out by applying the workflow TLS2trees (Wilkes et al. 2022) based on semantic classification approach, (Krisanski et al. 2021), that uses deep learning to classify a point cloud into leaf, wood, coarse woody debris and ground points. The deep learning model is applied 'as is' i.e. no additional pre-training is required Figure 4 shows the result of applying the TLS2trees workflow to TLS data from plot 1330.

Fig. 4. Trees extracted from the TLS survey of plot 1330.

Following the individual tree extraction, tree volume was estimated using the TreeQSM (version 2.3.1) (Raumonen et al. 2013). AGB at the level of single trees was then obtained based on published values of wood density taken from (Zianis et al., 2005). An allometric model of the form $a(D^2H)^b$was fitted to the TLS-derived estimates of biomass, where D and H are tree diameter at breast height (DBH) and height respectively. This model is a generic allometric form for tree volume and biomass estimation that has been used for deciduous European woodland (Wutzler et al. 2008) as well as more widely (Zianis et al, 2005). The resulting model was calibrated against the TLS-derived volume of 748 trees in total, covering the dominant species, across a wide size range, and at different growth stages). The

model takes the form $1.131(D^2H)^{0.857}$(r^2 = 0.96) and this subsequently used for the ALS-derived estimates of AGB.

4.1 Mobile Laser Scanning (MLS)

MLS data were collected during the TLS campaign in September 2021 and all TLS plots were covered. In contrast to TLS, where only few scan positions are visited, MLS systems are carried through the plot and thereby view the canopy from this trajectory. MLS acquisition time is much faster than TLS on the one hand. However, on the other hand, the range and power of these systems is often limited leading to low density in the upper canopy. At each plot, data were collected with a Greenvalley LiBackpack DGC50 in two successive walks. The raw ranging and Inertial Measurement Unit (IMU) data were processed with the provided Greenvalley software suite and resulting point clouds were registered to world coordinates based on the UAV-LS point clouds.

5. UAV Laser Scanning (UAV-LS)

UAV-LS data were acquired alongside the TLS data in September 2021. Two primary modes of acquisition were followed: first, coverage of all TLS plots in high density, cross-line patterns using one flight per plot. Second, flights that covered complete stands where the TLS plots were located (see figure 2). All flights were performed with a RIEGL VUX-1UAV and processing of raw sensor data to point clouds followed standardized procedures (Brede et al., 2017).

6. Airborne Laser Scanning (ALS)

Small footprint lidar ALS data were acquired by CzechGlobe in summer 2018 and remeasured in summer 2021. Lidar-derived products include terrain topography, forest height, and AGB estimates. Lidar-derived forest height is shown in figure 5.

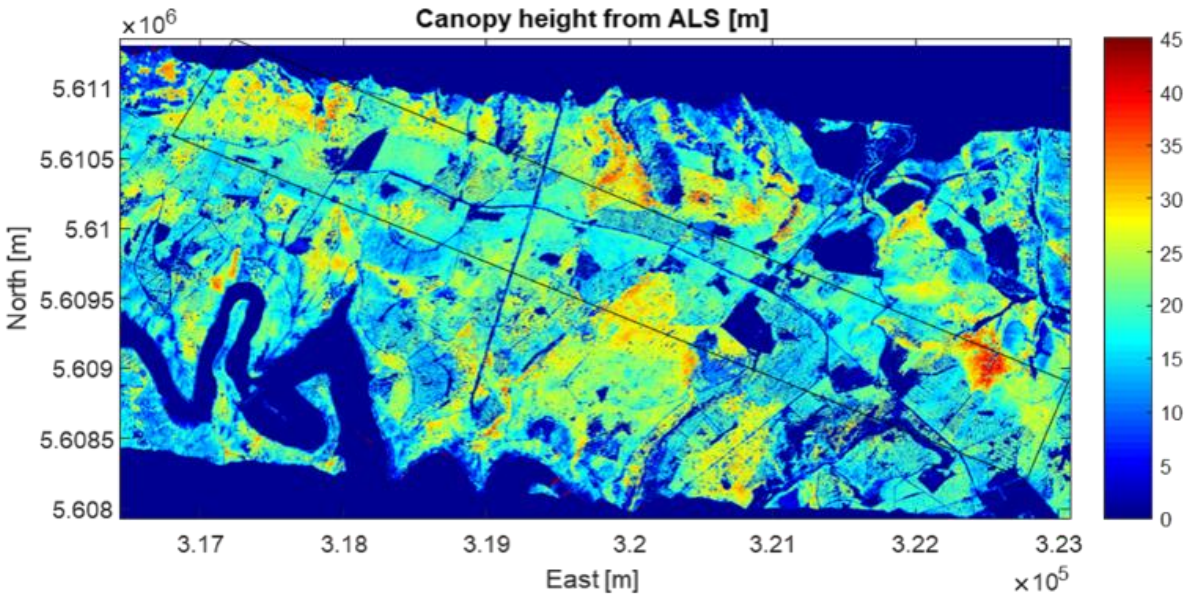

Fig. 5. Canopy Height Model (CHM) as derived from ALS data.

Spatial maps of forest AGB were produced by CzechGlobe based on data from the 80 forest census plots and corresponding AGB estimates derived using allometric equations based on analysis of TLS data (as described in section 4). The analysis was complemented by including information from additional 100 forest census plots from a previous study in the Silesian Beskids area at the border between Czech Republic and Poland, which is characterized by a similar species composition as in Kermeter. This choice was made to extend the biomass variability towards the low end, which is not well represented in Kermeter. Afterwards, plot data were partitioned into a training and validation sets, and used to train the coefficients of a number of predictors derived from ALS data through machine learning techniques (Brovkina et al., 2022). The top ten best performing models were averaged and the final robust meta-model was applied on predictors extracted in a regular grid to produce an AGB map in 10 m resolution.

7. SAR flights

SAR acquisitions were carried out by MetaSensing in July 2020 (P-band), September 2020 (L-band) and in November 2020 and October 2021 (C-band). All data were acquired by flying up to 30 times along two opposite headings (North-West and South-East), to provide vertical resolution capabilities

from two opposite views. L- and C-band data were acquired in bistatic mode by flying two identical SAR sensors onboard two aircraft. In so-doing, we obtained for each flight heading a mono-static (same sensor operated as transmitted and receiver) and a bi-static (one sensor as transmitter and the other as receiver) data-set. All data were collected in fully polarimetric mode, resulting in the collection of approximately one thousand SAR images.

All flights were performed using one or two Cessna 208 Grand Caravan, see figure 6, equipped with GPS antennas and a power supply panel. SAR calibration was supported with two 5 m trihedral reflectors for P-band installed by FOI, and two 75 cm ones for higher frequencies.

Fig. 6. The two Cessna 208 Grand Caravan used for the SAR flights.

P-Band trajectories were flown with constant altitude for the first 10 passes, and by progressively lowering the trajectory in the subsequent 10 passes. Trajectories at L- and C-Band were planned so that the second aircraft (Slave) follows the first one (Master) at a safe distance, reducing its altitude progressively at each flight. The relative position of the Slave aircraft w.r.t. the Master is referred to in jargon as *baseline*, and is commonly described in terms of its along-track and across-track components, as represented in figure 7.

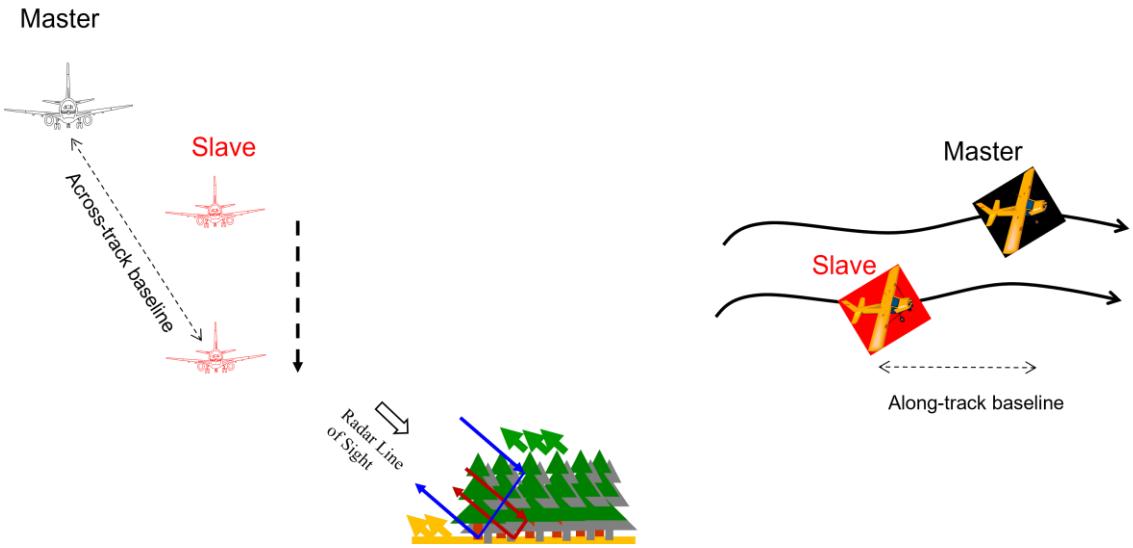

Fig. 7. Tomographic baselines. Master height is approximately 2000 m above the test site.

Unfortunately, the flight formation described above was not exactly implemented in 2020, resulting in the across-track baselines to be substantially larger than planned. At L-Band, the impact of large baselines was mitigated by the long wavelength, resulting in several single-pass interferograms where the signal associated with forest scattering is clearly detected and can be used for tomographic analysis. This was not the case at C-Band, and it was decided to fully re-fly the trajectories in October 2021 to ensure the presence of properly small and large baselines.

In all bistatic flights, safety conditions did not allow to fly at the planned along-track distance of 20 m. This resulted in an actual along-track distance between the two aircraft ranging from 50 m to 150 m, corresponding to a net delay between the images acquired by the two aircraft ranging from 0.5 s to 1.5 s. Relevant data parameters are summarized in Table 1 below.

	P-Band	L-Band	C-Band
Polarization	Full-pol	Full-pol	Full-pol
Bandwidth	30 MHz	50 MHz	100 MHz
Along-track resolution	≈ 1 m	≈ 1 m	≈ 0.6 m
Flight heading	North-West and South-East	North-West and South-East	North-West and South-East
Number of passes per heading	28 monostatic	30 monostatic 30 bistatic	17 monostatic 17 bistatic
Vertical resolution in the main area of interest	≈ 5 m to 10 m	< 5 m	< 5 m
Bistatic along track baseline	Not applicable	50 to 150 m	50 to 150 m

Table 1. Summary of SAR data

8. SAR processing and derived products

Radar processing was aimed at producing "tomographic cubes", i.e.: 3D voxels representing the complex scattering coefficients in 3D, with the height direction being relative to terrain topography (Tebaldini et al. 2017). To achieve this goal, several processing steps were needed.

In the first place, SAR data acquired along any single flight were focused by MetaSensing) directly in ground-coordinates, using terrain topography derived from ALS data and information about the platform trajectory from navigational data. The focusing processor corrects for amplitude factors related to distance variations and the antenna radiation pattern, in such a way as to directly associate image intensity with the backscatter coefficient (σ^0) in all polarizations. Despite that, however, the data had to be re-calibrated polarimetrically to fix some inconsistent features ascribed to the Radar system, which showed up mostly as offsets affecting the polarimetric phase and magnitudes in different flights. This problem was interpreted as being related to triggering and stopping the acquisition in each pass.

Accordingly, it was corrected under the assumption of a single distortion matrix per overpass, following the approach in (Villa et al., 2015). Afterwards, the polarimetric signature appeared to be uniform across all passes, and consistent with the expected features of forested areas.

Subsequent processing activities consisted in interferometric calibration and 3D focusing. As in most interferometric and tomographic campaigns, large part of calibration activities was aimed at correcting for mispositioning and phase errors due to inaccuracies of navigational data on the scale of a fraction of a wavelength (Tebaldini et al., 2016). This result was achieved in two steps. The first step consisted in the correction of azimuth shifts between different images, which was implemented following the multi-squint procedure proposed in (Reigber et al., 2006). The second calibration step was necessary to finely correct unwanted residual phase terms due to residual motion, which was implemented following the phase center double localization approach in (Tebaldini et. al, 2016). Calibrated SAR images were processed as described in (Yu et al., 2020) to generate 3D tomographic cubes. For an evaluation of the resulting imaging quality we refer the reader to section 8.1.

8.1 Tomographic imaging

We report a few examples to comment on the quality of TomoSense tomographic data. Figure 8 shows a tomographic transect, or *tomogram*, of the Kermeter forest as obtained by taking a vertical section from a P-Band tomographic cube (North-West heading, HH) and normalizing such that the sum over height is unitary for visualization purposes. The tomogram is visibly well focused, as it allows for a clear detection of the forest canopies and its lower envelope is very well correlated with ALS terrain topography (black line). The same transect is shown at HH and HV polarization in figure 9, where the vertical axis is now relative to ALS terrain elevation (i.e.: terrain topography is found at 0 m in each column). It is evident that the upper envelope of both tomograms is in very good agreement with ALS canopy height (white line). Interestingly, one can observe that ground scattering is dominant at HH, whereas canopy scattering is better detected at HV, consistently with observations in other forest biomes (Tebaldini et al., 2019).

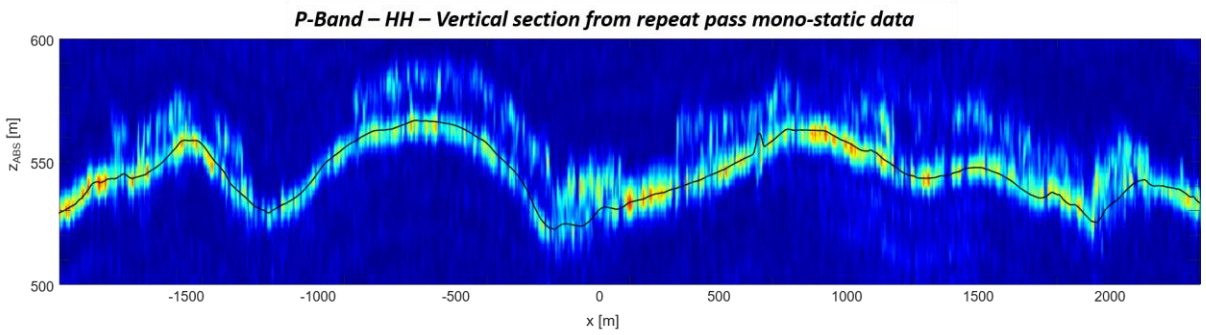

286

287 **Fig. 8**. P-Band tomography: vertical section (HH) in absolute coordinates. The black line overlaid
288 denotes terrain topography from ALS data.

289

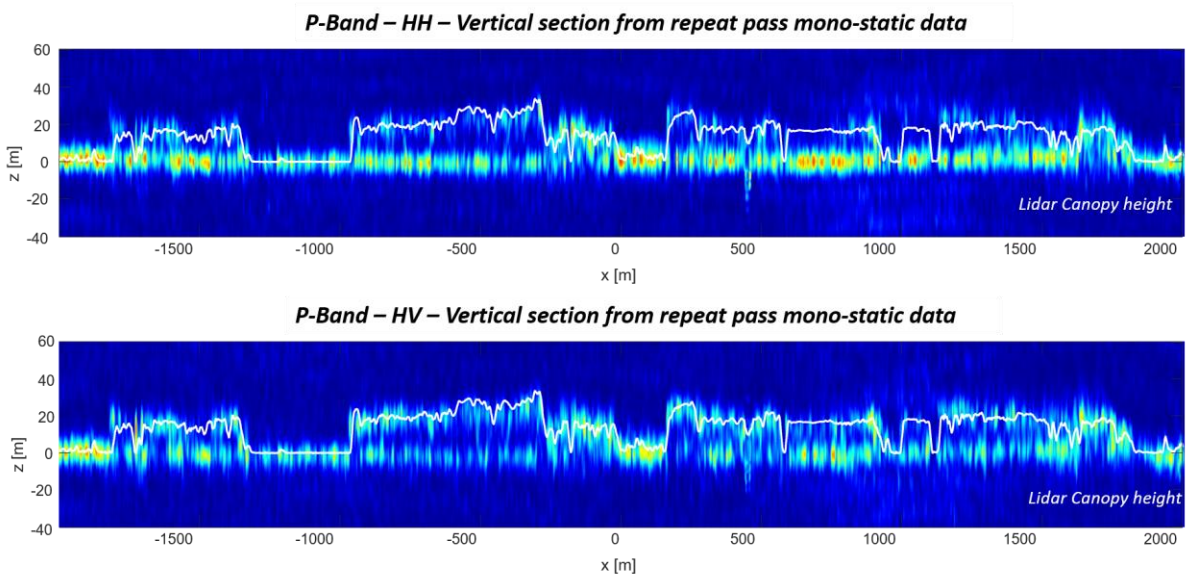

290

291 **Fig. 9**. P-Band tomography: vertical sections (HH and HV) w.r.t. terrain elevation (i.e.: terrain
292 topography is found at 0 m in each column). The white lines overlaid denotes canopy height from ALS
293 data.

294

295 L-band mono- and bi-static tomograms are shown in figure 10. Canopy scattering is dominant as
296 compared to P-Band, consistent with the physics of forest scattering. It is interesting to note that
297 scattering from the terrain level (at 0 m in figure 10) is weaker in the case of bi-static data (quantitative
298 analysis on the whole area shows an average decrease of about 4 dB w.r.t. mono-static data). This is
299 consistent with the finding in (Mariotti et al., 2013) that scattering from the ground level is largely

contributed by double-bounce interactions between the trunks and the terrain, resulting in large part of the scattered energy to return to the transmitter.

Figure 11 shows a comparison between L-Band bistatic Tomography and TLS at five plots sampled by with TLS. TLS data are represented by the average Plant Area Volume Density (PAVD), associated with the green curves, whereas tomographic data are represented by the average profile and are associated with the red curves. TLS and TomoSAR profiles are observed to exhibit a good agreement, especially for plots 1452, 1478, 1479. In plot 1399, the main peak is correctly detected by TomoSAR, but the understorey seems to be underestimated w.r.t. to the TLS profile. Viceversa, the top of the canopy is not detected by TomoSAR in plot 1330. Such discrepancies are to be ascribed to the use of radically different wavelength and vertical resolution. Another factor to account for is that the graphs in figure 11 are only representative of the average profiles within each plot, whereas more information could be retrieved by analysing the spatial variability of TomoSAR vertical profiles, as in (Pardini et al., 2018b).

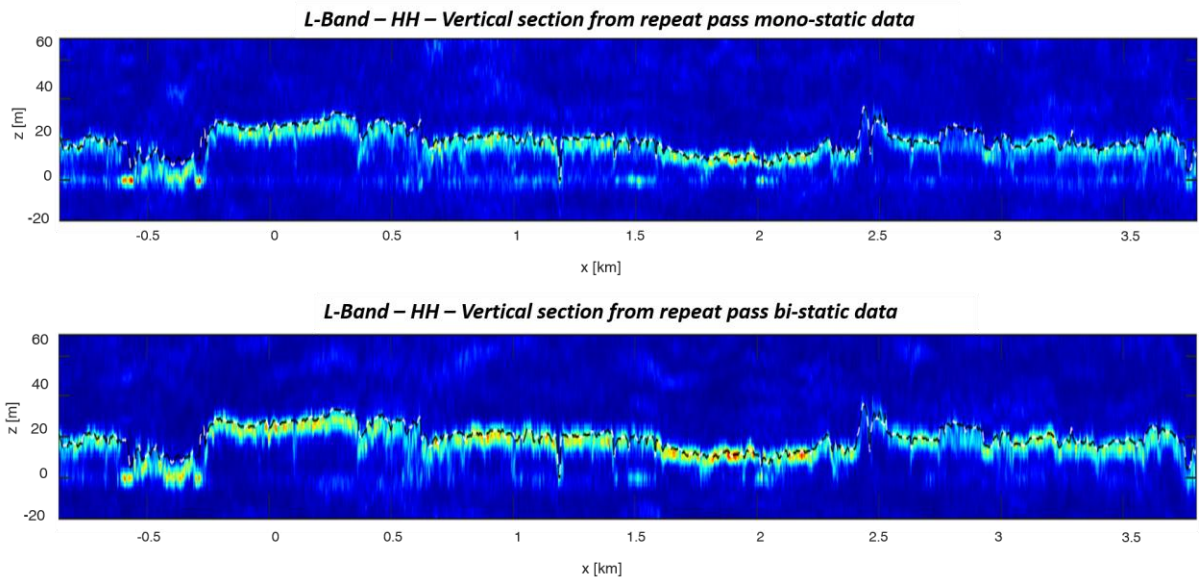

Fig. 10. L-Band tomography: vertical sections (mono-static and bistatic) w.r.t. terrain elevation. The dashed lines overlaid denotes canopy height from ALS data.

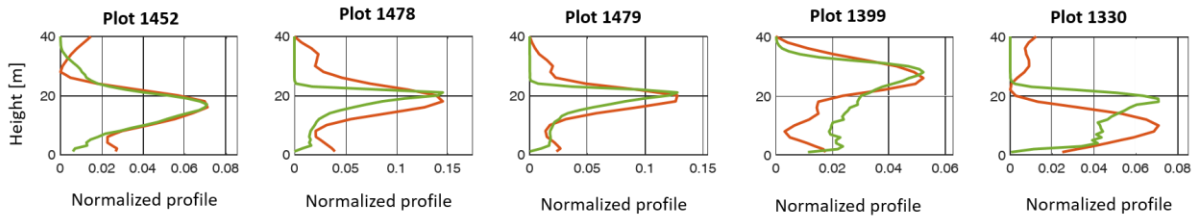

Fig. 11. Comparison between TLS and SAR Tomography at the five plots. Green curves: Plant Area Volume Density (PAVD, m^2/m^3) from TLS. Red curves: normalized tomographic profile from bistatic HV L-Band data (average over each plot).

Differently from L-Band, the signal from canopy scattering could not be detected in C-Band repeat pass data due to temporal decorrelation resulting from the time elapsed between consecutive flights (on the order of few minutes). A partial detection of the forest canopies is achieved by processing only image pairs acquired in the same pass (Tebaldini and Ferro-Famil, 2017), see figure 12. In this case, temporal decorrelation is only induced by the time lag between mono- and bi-static images from the same flight, which is slightly larger than the decorrelation time of canopy scattering at C-Band (Monteith and Ulander, 2022). Interestingly, the ground signal is here well detected, which demonstrates some penetration capabilities at C-Band as well.

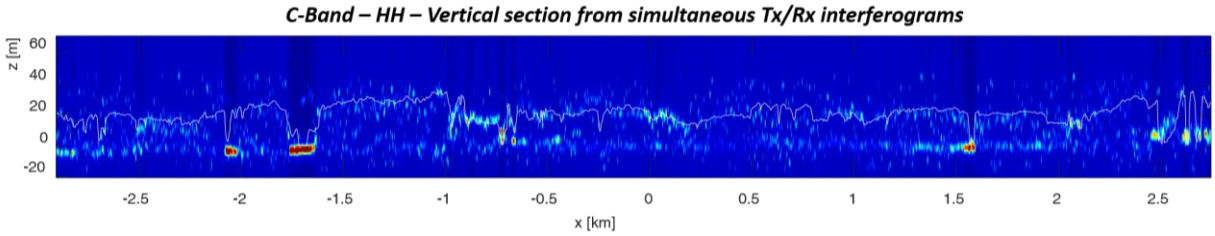

Fig. 12. C-Band tomography: vertical sections w.r.t. terrain elevation. The white lines overlaid denotes canopy height from ALS data.

9. Sensitivity to forest AGB

Figure 13 shows the L-band HV vertical reflectivity profiles for spruce and beech forest from the NW track bistatic acquisition. The profiles are based on 0.5 ha averages, i.e. the intensity is averaged over 0.5 ha in the horizontal for each height plane, which are then averaged over 20 t/ha AGB intervals. The curves are colored from low AGB (blue) to high AGB (red), to illustrate the AGB dependence. The

changing profiles for spruce and beech show a distinct difference when moving from low to high AGB. For spruce, the maximum intensity from the canopy is located at about 15-20 m and increases with AGB. For beech, on the other hand, the location of the maximum intensity increases from about 15 m to almost 30 m for increasing AGB, whereas the maximum value is almost constant.

The results using one AGB estimation method for temperate forest (a mix of all forest types) at P- and L-band NW track acquisition is shown in Figure 14. This method uses the fraction of the intensity in the 20 to 30 m height canopy layer to the total intensity of the vertical profile, for each 0.5 ha data point. Note that this is a normalized measure, allowing for comparison between points without absolute intensity calibration. The AGB is estimated through an exponential fit model, $A\hat{G}B = exp(a_0 + a_1 I_{dB})$ with parameters a_0 and a_1, estimated using the ALS AGB for half of the points as AGB reference data, i.e. training data, and the performance is evaluated using the remaining data points. . As seen, the results at L-band show an R^2 of 0.47 and an RMSE of 39.9 t/ha (15.6 %), while the results at P-band show an R^2 of 0.50 and an RMSE of 33.3 t/ha (12.7 %).

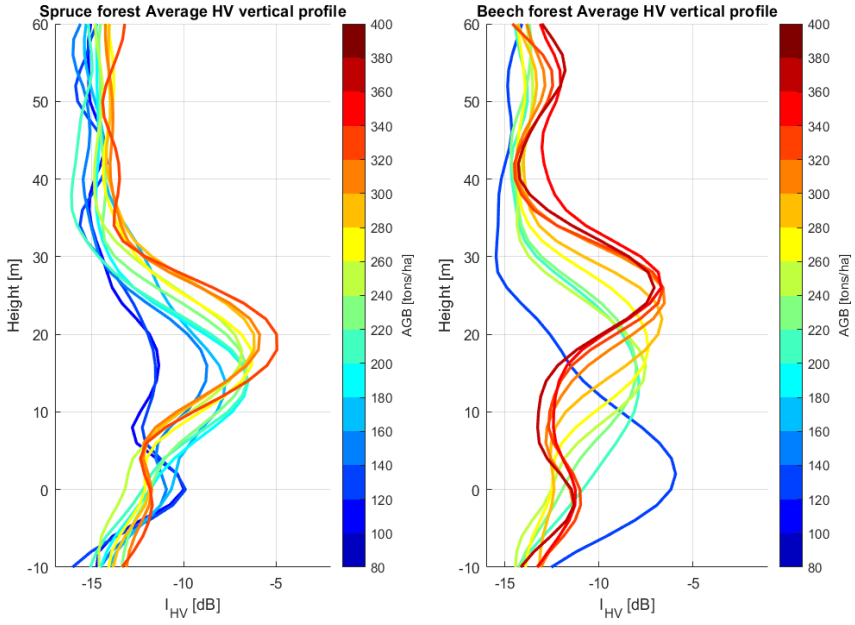

Fig. 13. Spruce and beech forest average L-band HV vertical reflectivity profiles for 0.5 ha points in 20 t/ha AGB intervals, from the NW track bistatic acquisition.

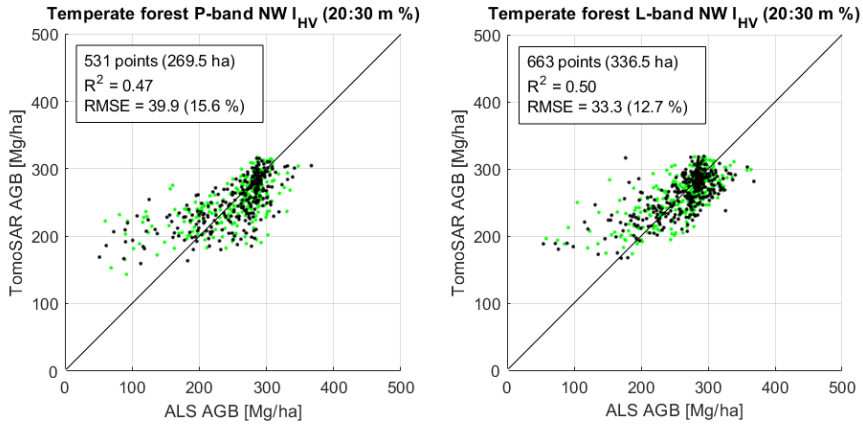

Fig. 14. P- and L-band NW track HV TomoSAR temperate forest (mix of all forest types) AGB estimation plotted against the reference ALS AGB, using every second point (shown in green) for training the exponential fit model. This is using the canopy layer fraction method (input is the fraction of the intensity in the 20 to 30 m canopy layer to the total intensity in the vertical reflectivity profile of each point).

With more than 500 data points used for the AGB retrieval at both P- and L-band, the RMSE and R^2 measures are considerably stable. Although, the density of data points is higher at high than at low AGB, pushing the mean AGB to the higher side of the covered interval. It should also be noted that the retrieval model tends to weight the estimate towards the mean AGB of the training data points for less than perfect correlation, minimizing the overall RMSE while overestimating low AGB and underestimating high AGB. This effect is apparent in the figures, in combination with the fact that a higher density of high than low AGB data points cause the model to fit high AGB better, in order to minimize the overall RMSE

10. Conclusions

The TomoSense experiment was conceived to provide key elements in support of the research on future SAR Missions focused on remote sensing of forested areas, such as the BIOMASS, NISAR, and

candidate bistatic missions like Tandem-L. To do that, an extensive data-set was collected comprising P., L-, C- Band data acquired in mono- and bi-static configurations, complemented by detailed terrestrial and aerial Lidar data and forest inventory. Results shown in this paper are only preliminary. Yet, they advocate for the vast range of analysis allowed by this data-set. It was shown that TomoSense provides accurate tomographic imaging of the vegetation at different wavelengths, polarizations, and observation modes, resulting in the possibility to compare Radar and Lidar observables and assess the retrieval of biophysical parameters on a quantitative basis. The entire dataset is free and openly available through ESA for research purposes and can be accessed at https://earth.esa.int/eogateway/catalog. Importantly, data are provided in a format that can be directly understood and used by researchers outside the Radar community. For this reason, we deem that TomoSense represents a unique opportunity for the scientific community to better understand the connection between forest biophysical parameters and Radar observables, and use this knowledge for the development of Earth Observation of forested areas.

Acknowledgements

This work was funded by the ESA under ESA/ESTEC contract No. 4000127285/19/NL/FF/gp. MD. PW acknowledge capital funding for TLS equipment from UCL Geography and the NERC National Centre for Earth Observation (NCEO). The WUR TLS and UAV-LS campaign was funded by the ESA IDEAS-QA4EO project contract No. 4000128960/19/I-NS.

References

Aghababaei, H., Ferraioli, G., Ferro-Famil, L., Huang, Y., Mariotti D'Alessandro, M., Pascazio, V., Schirinzi, G., Tebaldini, S. Forest SAR Tomography: Principles and Applications (2020) IEEE Geoscience and Remote Sensing Magazine, 8 (2), art. no. 8995799, pp. 30-45

Azcueta, M., Tebaldini, S. Potential for Absolute Ionosphere and Clock Correction in Noncooperative Bistatic SAR (2020) IEEE Transactions on Geoscience and Remote Sensing, 58 (1), art. no. 8844297, pp. 363-377

Blomberg, E., Ulander, L.M.H., Tebaldini, S., Ferro-Famil, L.Evaluating P-Band TomoSAR for Biomass Retrieval in Boreal Forest (2021) IEEE Transactions on Geoscience and Remote Sensing, 59 (5), art. no. 9204469, pp. 3793-3804.

Boni Vicari, M., Disney, M. I., Wilkes, P., Burt, A., Calders, K. and Woodgate, W. (2019) New framework for separating leaf and wood in terrestrial LiDAR point clouds, Methods in Ecology and Evolution, DOI: 10.1111/2041-210X.13144.

Brede, B., Lau, A., Bartholomeus, H. M., and Kooistra, L. (2017) Comparing RIEGL RiCOPTER UAV LiDAR Derived Canopy Height and DBH with Terrestrial LiDAR, Sensors, 17(10), 2371, doi: 10.3390/s17102371.

Brede, B., Terryn, L., Barbier, N., Bartholomeus, H. M., Bartolo, R., Calders, K., Derroire, G., Krishna Moorthy, S. M., Lau, A., Levick, S. R., Raumonen, P., Verbeeck, H., Wang, D., Whiteside, T., van der Zee, J., & Herold, M. (2022). Non-destructive estimation of individual tree biomass: Allometric models, terrestrial and UAV laser scanning. Remote Sensing of Environment, 280, 113180. DOI:10.1016/j.rse.2022.113180

Brovkina, O.; Navrátilová, B.; Novotný, J.; Albert, J.; Slezák, L.; Cienciala, E. (2022) Influences of vegetation, model, and data parameters on forest aboveground biomass assessment using an area-based approach. Ecological Informatics 2022(70): 1-12, Article number 101754.

Burt, A., Disney, M. I. and Calders, K. (2019) Extracting individual trees from lidar point clouds using treeseg, Methods in Ecology and Evolution, https://doi.org/10.1111/2041-210X.13121.

Disney, M. I. (2018) Terrestrial LiDAR: a 3D revolution in how we look at trees, New Phytologist, doi.org/10.1111/nph.15517.

Disney, M. I., et al. (2018) Weighing trees with lasers: advances, challenges and opportunities, Royal Society Interface Focus 8 (2), Special Issue on Royal Society meeting 'The terrestrial laser scanning revolution in forest ecology', doi: 10.1098/rsfs.2017.0048.

El Moussawi, I., Minh, D.H.T., Baghdadi, N., Abdallah, C., Jomaah, J., Strauss, O., Lavalle, M., Ngo, Y.-N. (2019) Monitoring tropical forest structure using SAR tomography at L- and P-band Remote Sensing, 11 (16), art. no. 1934.

Fatoyinbo, T., et al., (2021) The NASA AfriSAR campaign: Airborne SAR and lidar measurements of tropical forest structure and biomass in support of current and future space missions, Remote Sensing of Environment, 264, art. no. 112533,

Frey, O., Morsdorf, F., Meier, E. (2008) Tomographic imaging of a forested area by airborne multi-baseline P-band SAR, Sensors, 8 (9), pp. 5884-5896.

Ho Tong Minh, D., Le Toan, T., Rocca, F., Tebaldini, S., D'Alessandro, M.M., Villard, L. (2014) Relating P-band synthetic aperture radar tomography to tropical forest biomass, IEEE Transactions on Geoscience and Remote Sensing, 52 (2), art. no. 6488809, pp. 967-979.

Ho Tong Minh, D., Le Toan, T., Rocca, F., Tebaldini, S., Villard, L., Réjou-Méchain, M., Phillips, O.L., Feldpausch, T.R., Dubois-Fernandez, P., Scipal, K., Chave, J. (2016) SAR tomography for the retrieval of forest biomass and height: Cross-validation at two tropical forest sites in French Guiana, Remote Sensing of Environment, 175, pp. 138-147.

Khati, U., Lavalle, M., Singh, G. (2019) Spaceborne tomography of multi-species Indian tropical forests, Remote Sensing of Environment, 229, pp. 193-212.

Krisanski, S., Taskhiri, M.S., Gonzalez Aracil, S., Herries, D. and Turner, P., (2021) Sensor Agnostic Semantic Segmentation of Structurally Diverse and Complex Forest Point Clouds Using Deep Learning. Remote Sensing, 13(8), p.1413.

Mariotti D'Alessandro, M., Tebaldini, S., Quegan, S., Soja, M.J., Ulander, L.M.H., Scipal, K. (2020) Interferometric Ground Cancellation for above Ground Biomass Estimation, IEEE Transactions on Geoscience and Remote Sensing, 58 (9), art. no. 9033990, pp. 6410-6419.

Mariotti D'Alessandro, M., Tebaldini, S. (2019) Digital terrain model retrieval in tropical forests through P-Band SAR tomography, IEEE Transactions on Geoscience and Remote Sensing, 57 (9), art. no. 8701518, pp. 6774-6781

Mariotti d'Alessandro, M. Tebaldini S., Rocca, F., (2013) Phenomenology of Ground Scattering in a Tropical Forest Through Polarimetric Synthetic Aperture Radar Tomography, IEEE Transactions on Geoscience and Remote Sensing, vol. 51, no. 8, pp. 4430-4437, Aug. 2013,

Mokroš, M., Mikita, T., Singh, A., Tomaštík, J., Chudá, J., Wężyk, P., Kuželka, K., Surový, P., Klimánek, M., Zięba-Kulawik, K., Bobrowski, R., & Liang, X. (2021). Novel low-cost mobile mapping systems for forest inventories as terrestrial laser scanning alternatives. International Journal of Applied Earth Observation and Geoinformation, 104, 102512. DOI:10.1016/j.jag.2021.102512

Monteith A. R. and Ulander, L. M. H., (2022), A Tower-Based Radar Study of Temporal Coherence of a Boreal Forest at P-, L-, and C-Bands and Linear Cross Polarization, in IEEE Transactions on Geoscience and Remote Sensing, vol. 60, pp. 1-15, 2022, Art no. 4402315, doi: 10.1109/TGRS.2021.3074098.

Moreira, A. et al., (2015) Tandem-L: A Highly Innovative Bistatic SAR Mission for Global Observation of Dynamic Processes on the Earth's Surface, IEEE Geoscience and Remote Sensing Magazine, vol. 3, no. 2, pp. 8-23, June 2015, doi: 10.1109/MGRS.2015.2437353.

Orban, A., and Defrere D., Barbier, C., (2021) BelSAR : the first Belgian airborne campaign for L-band, full polarimetric bistatic and interferometric SAR acquisitions over an agricultural site in Belgium, EUSAR 2021; 13th European Conference on Synthetic Aperture Radar, *2021, pp. 1-4.*

Pardini, M., Papathanassiou, K.P., Lombardini, F. (2018) Impact of dielectric changes on L-band 3-d SAR reflectivity profiles of forest volumes, IEEE Transactions on Geoscience and Remote Sensing, 56 (12), art. no. 8424543, pp. 7324-7337.

M. Pardini, M. Tello, V. Cazcarra-Bes, K. P. Papathanassiou and I. Hajnsek, "L- and P-Band 3-D SAR Reflectivity Profiles Versus Lidar Waveforms: The AfriSAR Case," in *IEEE Journal of Selected Topics in Applied Earth Observations and Remote Sensing*, vol. 11, no. 10, pp. 3386-3401, Oct. 2018, doi: 10.1109/JSTARS.2018.2847033.

Quegan, S., Le Toan, T., Chave, J., Dall, J., Exbrayat, J.-F., Minh, D.H.T., Lomas, M., D'Alessandro, M.M., Paillou, P., Papathanassiou, K., Rocca, F., Saatchi, S., Scipal, K., Shugart, H., Smallman, T.L., Soja, M.J., Tebaldini, S., Ulander, L., Villard, L., Williams, M. (2019) The European Space Agency BIOMASS mission: Measuring forest above-ground biomass from space, Remote Sensing of Environment, 227, pp. 44-60.

Raumonen, P., Kaasalainen, M., Åkerblom, M., Kaasalainen, S., Kaartinen, H., Vastaranta, M., Holopainen, M., Disney, M. and Lewis, P., (2013) Fast automatic precision tree models from terrestrial laser scanner data, Remote Sensing, 5(2), pp.491-520.

Reigber A., Moreira A., (2000) First demonstration of airborne SAR tomography using multibaseline L-band data, IEEE Transactions on Geoscience and Remote Sensing, vol. 38, no. 5, pp. 2142,2152, Sep 2000.

Reigber, A., Prats P., and Mallorqui, J. J., (2006) Refined estimation of time-varying baseline errors in airborne SAR interferometry, IEEE Geoscience and Remote Sensing Letters, vol. 3, no. 1, pp. 145-149, Jan. 2006.

490 Scipal, K. and Davidson, M., (2017) The SAOCOM-CS mission: ESA's first bistatic and tomographic
491 L-band mission, 2017 IEEE International Geoscience and Remote Sensing Symposium (IGARSS),
492 2017, pp. 123-124.

493 Siegmann, B., et al: (2019) The High-Performance Airborne Imaging Spectrometer HyPlant—From
494 Raw Images to Top-of-Canopy Reflectance and Fluorescence Products: Introduction of an Automatized
495 Processing Chain, Remote Sens. 2019, 11, 2760.

496 Soja, M.J., Quegan, S., d'Alessandro, M.M., Banda, F., Scipal, K., Tebaldini, S., Ulander, L.M.H.
497 (2021) Mapping above-ground biomass in tropical forests with ground-cancelled P-band SAR and
498 limited reference data, Remote Sensing of Environment, 253, art. no. 112153.

499 Tebaldini, S., Ho Tong Minh, D., Mariotti d'Alessandro, M., Villard, L., Le Toan, T., Chave, J.
500 (2019) The Status of Technologies to Measure Forest Biomass and Structural Properties: State of the
501 Art in SAR Tomography of Tropical Forests, Surveys in Geophysics, 40 (4), pp. 779-801.

502 Tebaldini, S., Rocca, F., Mariotti D'Alessandro, M., Ferro-Famil, L. (2016) Phase calibration of
503 airborne tomographic SAR data via phase center double localization, IEEE Transactions on
504 Geoscience and Remote Sensing, 54 (3), art. no. 7308057, pp. 1775-1792.

505 Tebaldini S., Ferro-Famil, L. (2017) SAR tomography from bistatic single-pass interferometers, 2017
506 IEEE International Geoscience and Remote Sensing Symposium (IGARSS), 2017, pp. 133-136,

507 Tello, M., Cazcarra-Bes, V., Pardini, M., Papathanassiou, K. (2018) Forest structure characterization
508 from SAR tomography at L-band, IEEE Journal of Selected Topics in Applied Earth Observations and
509 Remote Sensing, 11 (10), art. no. 8457291, pp. 3402-3414.

510 Toraño Caicoya, A., Pardini, M., Hajnsek, I., Papathanassiou, K. (2015) Forest Above-Ground Biomass
511 Estimation From Vertical Reflectivity Profiles at L-Band, IEEE Geoscience and Remote Sensing
512 Letters, 12 (12), art. no. 7305772, pp. 2379-2383

513 Villa, A., Iannini, L., Giudici, D., Monti-Guarnieri, A., Tebaldini, S. (2015) Calibration of SAR
514 polarimetric images by means of a covariance matching approach IEEE Transactions on Geoscience
515 and Remote Sensing, 53 (2), art. no. 6834807, pp. 674-686.

516 Wilkes, P., Lau, A., Disney, M., Calders, K., Burt, A., de Tanago, J.G., Bartholomeus, H., Brede, B.
517 and Herold, M., (2017) Data acquisition considerations for terrestrial laser scanning of forest
518 plots,Remote Sensing of Environment, 196, pp.140-153.

519 Wilkes, P., Disney, M.I., Armston, J., Bartholomeus, H., Bentley, L.P., Brede, B., Burt, A., Calders,
520 K., Chavana-Bryant, C., Clewley, D. and Duncanson, L. (2022) TLS2trees: a scalable tree
521 segmentation pipeline for TLS data. *bioRxiv*; https://doi.org/10.1101/2022.12.07.518693

522 Wutzler, T., Wirth, C. and Schumacher, J. (2008) Generic biomass functions for Common beech
523 (Fagus sylvatica) in Central Europe: predictions and components of uncertainty, Canadian Journal of
524 Forest Research, 38(6), pp. 1661–1675 (2008) doi: 10.1139/X07-194

525 Yu, Y., d'Alessandro, M.M., Tebaldini, S., Liao, M. (2020) Signal processing options for high
526 resolution SAR tomography of natural scenarios Remote Sensing, 12 (10), art. no. 1638, .

527 Zianis, D., Muukkonen, P., Makipaa, R., & Mencuccini, M. (2005). Biomass and stem volume
528 equations for tree species in Europe. Silva Fennica monographs, (4), 1-2,5-63